PAPER

ABPO-TVSCAD: alternating Bregman proximity operators approach based on TVSCAD regularization for bioluminescence tomography

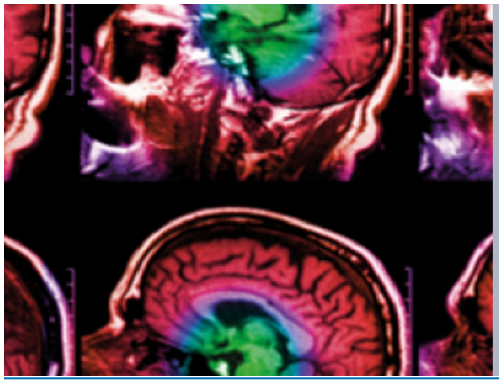

IOP Publishing Phys. Med. Biol. 67 (2022) 215013 https://doi.org/10.1088/1361-6560/ac994c

Physics in Medicine & Biology

IPEM Institute of Physics and Engineering in Medicine

RECEIVED
26 July 2022

REVISED
1 September 2022

ACCEPTED FOR PUBLICATION
11 October 2022

PUBLISHED
27 October 2022

PAPER

ABPO-TVSCAD: alternating Bregman proximity operators approach based on TVSCAD regularization for bioluminescence tomography

Yi Chen[1], Mengfei Du[1], Weitong Li[1], Linzhi Su[1,*], Huangjian Yi[1], Fengjun Zhao[1], Kang Li[1], Lin Wang[2] and Xin Cao[1,*]

[1] School of Information Sciences and Technology, Northwest University, Xi'an 710127, People's Republic of China
[2] School of Computer Science and Engineering, Xi'an University of Technology, Xi'an 710048, People's Republic of China
[*] Authors to whom any correspondence should be addressed.

E-mail: sulinzhi029@163.com **and** xin_cao@163.com

Keywords: bioluminescence tomography, TVSCAD, Bregman proximity operators, inverse problems

Abstract

Objective. Bioluminescence tomography (BLT) is a promising non-invasive optical medical imaging technique, which can visualize and quantitatively analyze the distribution of tumor cells in living tissues. However, due to the influence of photon scattering effect and ill-conditioned inverse problem, the reconstruction result is unsatisfactory. The purpose of this study is to improve the reconstruction performance of BLT. *Approach.* An alternating Bregman proximity operators (ABPO) method based on TVSCAD regularization is proposed for BLT reconstruction. TVSCAD combines the anisotropic total variation (TV) regularization constraints and the non-convex smoothly clipped absolute deviation (SCAD) penalty constraints, to make a trade-off between the sparsity and edge preservation of the source. ABPO approach is used to solve the TVSCAD model (ABPO-TVSCAD for short). In addition, to accelerate the convergence speed of the ABPO, we adapt the strategy of shrinking the permission source region, which further improves the performance of ABPO-TVSCAD. *Main results.* The results of numerical simulations and *in vivo* xenograft mouse experiment show that our proposed method achieved superior accuracy in spatial localization and morphological reconstruction of bioluminescent source. *Significance.* ABPO-TVSCAD is an effective and robust reconstruction method for BLT, and we hope that this method can promote the development of optical molecular tomography.

1. Introduction

Bioluminescence imaging (BLI) is a highly sensitive, non-invasive, non-ionizing optical molecular imaging method, which has played an increasingly important role in preclinical research of small animals. By utilizing an ultra-sensitive CCD camera to detect the visible and near-infrared light emitted by luminous imaging probes in living cells, BLI allows researchers to monitor cell growth and localize tumors in small animals (Massoud and Gambhir 2003, Ntziachristos 2010, Wu *et al* 2013). Up to now, BLI has been widely used in medical fields such as early tumor detection, drug development, and surgical guidance (Wenxiang *et al* 2005, Ma *et al* 2011, Xu *et al* 2021). However, due to the serious scattering effect of light in biological tissue, BLI image cannot provide the depth information of the bioluminescence source in tissue (Feng *et al* 2011). Therefore, bioluminescence tomography (BLT) was proposed to address the problem of insufficient depth resolution (Yin *et al* 2021). Specifically, BLT can recover the spatial information of the bioluminescent sources through complex reconstruction algorithms, which makes the positioning of internal bioluminescent sources and quantitative analysis of bioluminescent density more accurate (Wang *et al* 2004, Klose *et al* 2010, Darne *et al* 2013). BLT employs the forward photon propagation model, and combined with the optimization algorithm, the bioluminescent flux on the surface of the organism is used to model-based inverse reconstruct the source distribution (Dehghani *et al* 2018). However, the light scattering and the limitation of detected photons result in

the high ill-posedness of the BLT, so it is extremely challenging to reconstruct the source distribution (Qin *et al* 2014, Feng *et al* 2018, Guo *et al* 2018). Therefore, it is necessary to design effective and robust reconstruction methods to alleviate the ill-posed problem.

In the past decade, researchers have designed effective solutions and used different effective prior information to reduce ill-posedness and stabilize the solution. Wang *et al* first theoretically proved that the ill-posedness can be alleviated by incorporating sufficient prior information, and the solution can be obtained uniquely and accurately (Wang *et al* 2004). Some regularization methods have also been proposed and applied to BLT reconstruction, such as L_2-norm regularization. However, the method based on L_2-norm will cause excessive smoothing and artifacts in the reconstructed image (Han *et al* 2006, Gong *et al* 2018). Based on compressed sensing theory (Baraniuk *et al* 2010), a variety of sparse algorithms have been proposed to solve the problem of optical tomography (e.g. L_0 and L_1) (Naser and Patterson 2010, Qin *et al* 2011), including incomplete variables truncated conjugate gradient method (He *et al* 2010), stagewise fast LASSO (Yu *et al* 2010), sparse Bayesian approach (Yin *et al* 2019), and so forth. These sparse regularization algorithms can overcome the over-smoothing defect of L_2 norm, but reduce the reconstruction accuracy and shape recovery ability of BLT (Guo *et al* 2020).

In recent years, deep learning has attracted attention in various fields, and some researchers have tried to apply deep learning to optical tomography reconstruction. In 2018, Gao *et al* designed an inverse problem simulations based on multilayer perceptrons to perform high-resolution BLT (Gao *et al* 2018). Subsequently, Guo *et al* proposed a reconstruction scheme based on 3D Encoder (Guo *et al* 2019), Huang *et al* proposed a recurrent neural network solution (Huang *et al* 2019), and Li *et al* proposed an end-to-end BLT reconstruction strategy based on convolution neural network (Li *et al* 2021). Because the deep learning methods train on the large dataset and establish the mapping from input to output, it can avoid the inaccuracy of the forward photon propagation modeling and ill-posed inverse problem (Li *et al* 2020). However, its generalization ability is weak, so the trained artificial neural network can only be applied to specific imaging objects (Cao *et al* 2019).

For image-guided surgery of BLT, the boundaries of the tumor and other tissues are of paramount importance. For this reason, the preservation of boundary information and morphological features is also necessary for BLT reconstruction (Guo *et al* 2022). Total variation (TV) regularization has been applied to various medical image reconstructions, and it can preserve image edge information well (Hintermüller *et al* 2018), but some authors have shown that TV regularization can produce some blocking artifacts in medical image reconstruction (Ring 2000, Herman and Davidi 2008). To address these limitations of TV regularization, the smoothly clipped absolute deviation (SCAD) (Fan and Li 2001) penalty has been proposed by Fan and Li. SCAD has become quite popular in the statistical community and has shown some desirable properties such as continuity, asymptotic unbiasedness, and sparsity (Wang *et al* 2015). However, there are few applications of SCAD in medical image reconstruction.

In this work, an alternating Bregman proximity operators (ABPO) method based on TVSCAD regularization was proposed for BLT reconstruction. The SCAD penalty of non-convex TV regularization is utilized as the regularization term, to balance sparsity and edge preservation of bioluminescent sources. The bioluminescent source distribution is non-negativity, so a non-negativity constraint is added to the TVSCAD model. Inspired by the split Bregman algorithm (Wang *et al* 2012), we design the ABPO algorithm, which splits the non-differentiable term and the data fidelity term to iteratively solve the TVSCAD model. Meanwhile, to reduce the ill-posed problem and improve the accuracy of the reconstructed source, a shrinking permission source region strategy (PSR) (Yang *et al* 2018) is used. We performed numerical simulations and *in vivo* xenograft mouse experiment to evaluate the performance of ABPO-TVSCAD. The results revealed that ABPO-TVSCAD not only achieves superior position and shape recovery accuracy, but also has strong robustness.

The rest of this paper is structured as follows: The specific details of ABPO-TVSCAD are demonstrated in section 2. Section 3 introduces the conditions of the simulations experiments and xenotransplantation experiments, and compares and validates the experimental results of different methods. We provide some discussion and summary of this paper in section 4.

2. Methods

The radiative transfer equation (RTE), also known as the linear Boltzmann equation, is used to describe the propagation of photons in tissue (Klose and Larsen 2006). But it is nearly impossible to find the solution of RTE. So, the diffusion equation has been developed to overcome the difficulties of solving RTE. It is a simplified first-order approximation of the RTE, which has been used to simulate light propagation in biological tissue (Cong and Wang 2006, Leng and Tian 2015). It is defined as:

$$-\nabla(D_c(r)\nabla\phi(r)) + \mu_a(r)\phi(r) = S(r), \quad r \in \Omega, \tag{1}$$

where r is the position vector, $D_c(r)$ is the diffusion coefficient of position vector r, μ_a is the absorption coefficient, $\phi(r)$ is the photon flux density of position vector r, $S(r)$ is the internal source distribution of position vector r, and Ω is the region of the biological tissue. D_c is calculated as follows:

$$D_c = \frac{1}{3(\mu_a + (1-g)\mu_s)}, \tag{2}$$

where g represents the anisotropy parameter, and μ_s is scattering coefficient. Diffusion equation combined with the Robin boundary condition (Jianghong *et al* 2011, Wu *et al* 2012), expressed as follows:

$$\phi(r) + 2F_{bm}(r; n, n')D_c(r)(v(r)\nabla \phi(r)) = 0, \quad r \in \partial\Omega, \tag{3}$$

where F_{bm} is the boundary mismatch factor between the biological tissues and the surrounding medium, n is the refractive indices within $\partial\Omega$, n' is the refractive indices of the surrounding medium, $\partial\Omega$ denotes the boundary of biological tissue, and v is the unit outward normal on $\partial\Omega$.

The outgoing photon density on the biological tissue boundary $\partial\Omega$ is expressed as follows:

$$\Gamma(r) = -D_c(r)(v(r)\nabla\phi(r)) = \frac{\phi(r)}{2F_{bm}(r; n, n')}, r \in \partial\Omega. \tag{4}$$

The finite element method is applied to the photon diffusion model, and the linear relationship between the measured photon flux B and the unknown source density X is established as follows:

$$AX = B, \tag{5}$$

where $A \in \mathbb{R}^{N\times N}$ is the system matrix, and N is the number of the discretized nodes.

2.1. TVSCAD model

The inverse problem of equation (5) is a well-known ill-posed problem, and only meaningless solutions can be obtained by standard numerical methods. Therefore, we propose a TVSCAD model to reduce its ill-posedness and obtain a sparse and meaningful solution. Here, the traditional BLT objective function based on TVSCAD model can be expressed as:

$$\min_{X\in\mathbb{R}} E(X) = \frac{1}{2}\|AX - B\|_2^2 + \lambda \|X\|_{TVSCAD}, \tag{6}$$

where $E(X)$ denotes the objective function, λ is the positive regularization parameter, $\|\cdot\|_2^2$ denotes L_2-norm, and $\|X\|_{TVSCAD}$ is TVSCAD regularization. The TVSCAD term in equation (6) will be mathematically derived in detail as follows.

Using finite difference operation, we can discretize TV into different forms. The isotropic discretization TV_{iso} and anisotropic discretization TV_{ani} of TV are given by the following formula:

$$TV_{iso}(X) = \|DX\|_2^2 \text{ and } TV_{ani}(X) = \|DX\|, \tag{7}$$

where D is the finite difference operator, and $\|\cdot\|$ denotes L_1-norm. In this work, we have chosen anisotropic discretization of TV according to Wang *et al* (2017). In practice, anisotropic TV is slightly easier to process than isotropic TV (Gu *et al* 2017).

The SCAD function was originally introduced in literature Fan and Li (2001) as a penalty function for sparse variable selection, and it is defined as follows:

$$\varphi_\gamma(x) = \begin{cases} |x|, & |x| \leqslant \gamma_1 \\ \dfrac{2\gamma_2|x| - x^2 - \gamma_1^2}{2(\gamma_2 - \gamma_1)}, & \gamma_1 < |x| < \gamma_2, \\ \dfrac{\gamma_1 + \gamma_2}{2}, & |x| \geqslant \gamma_2 \end{cases} \tag{8}$$

where $\Phi_\gamma(x)$ is the SCAD function, γ_1 and γ_2 are the threshold parameters and satisfy $\gamma_2 > \gamma_1 > 0$. Let γ: $=(\gamma_1, \gamma_2)$, and $\gamma_2 = a\gamma_1 (a = 3.7)$ (Fan and Li 2001). The graph of $\Phi_\gamma(x)$ is shown in figure 1(a).

According to the definition of the SCAD function, we define another function $\psi(x)$ as following:

$$\psi_\gamma(x) = |x| - \Phi_\gamma(x) = \begin{cases} 0, & |x| \leqslant \gamma_1 \\ \dfrac{x^2 + \gamma_1^2 - 2\gamma_1|x|}{2(\gamma_2 - \gamma_1)}, & \gamma_1 < |x| < \gamma_2. \\ |x| - \dfrac{\gamma_1 + \gamma_2}{2}, & |x| \geqslant \gamma_2 \end{cases} \tag{9}$$

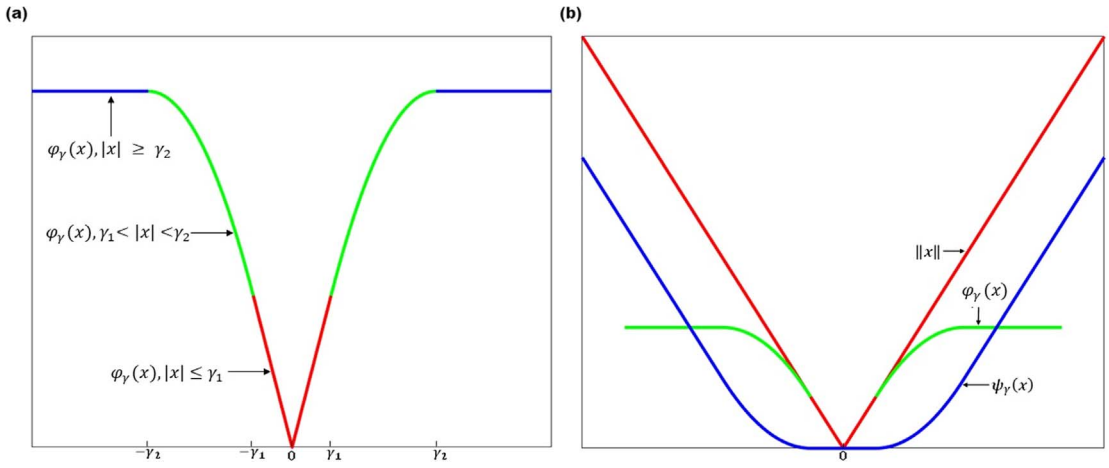

Figure 1. (a) Shows the SCAD function, (b) shows the decomposition of the SCAD.

The graph of $\psi(x)$ is illustrated in figure 1(b). Apparently, the function $\psi(x)$ is convex, differentiable, and satisfied $0 < \psi(x) < |x|$.

For BLT reconstruction, we define corresponding multivariate functions φ_γ as follows:

$$\Phi_\gamma(V) = \sum_{i=1}^{N} \varphi_\gamma(v_i), \quad V \epsilon \mathbb{R}^{\mathbb{N}}. \tag{10}$$

The component-wise extension function ψ_γ is given by:

$$\Psi_\gamma(V) = \sum_{i=1}^{N} \psi_\gamma(v_i), \quad V \epsilon \mathbb{R}^{\mathbb{N}}, \tag{11}$$

here, for all the $V \in \mathbb{R}^{\mathbb{N}}$, $\Psi_\gamma(V) = \|V\| - \Phi_\gamma(V)$. Then, let the gradient DX replace v in the above-mentioned equation. The definition of TVSCAD penalty is as follows:

$$\|X\|_{TVSCAD} = \Phi_\gamma(DX) = \|DX\| - \Psi_\gamma(DX), \tag{12}$$

where $D \in \mathbb{R}^{N-1*N}$ is the first-order difference matrix.

Therefore, the objective function equation (6) can be reformulated as the following:

$$\min_{X \in \mathbb{R}} E(X) = \frac{1}{2} \|AX - B\|_2^2 + \lambda \Phi_\gamma(DX) = \frac{1}{2} \|AX - B\|_2^2 + \lambda(\|DX\| - \Psi_\gamma(DX)). \tag{13}$$

This formula is TVSCAD model.

2.2. ABPO-TVSCAD algorithm

It is obvious that Φ_γ is non-convex and non-smooth, so the TVSCAD model is non-convex and non-smooth. The use of non-convex and non-smooth functions in image reconstruction usually leads to better contrast and clearer edges (Gu *et al* 2017). Inspired by the split Bregman algorithm, to solve the TVSCAD model, a new auxiliary variable $Z = DX$ is introduced, so equation (13) can be expressed as a constrained optimization problem:

$$\min_{X,Z} E(X) = \frac{1}{2} \|AX - B\|_2^2 + \lambda \Phi_\gamma(Z), \quad \textit{subject to } Z = DX, \tag{14}$$

where $\Phi_\gamma(Z) = \|Z\| - \Psi_\gamma(Z)$. The unconstrained optimization problem corresponding to equation (14) can be expressed as:

$$\min_{X,Z} E(X) = \frac{1}{2} \|AX - B\|_2^2 + \lambda \Phi_\gamma(Z) + \frac{\eta}{2} \|Z - DX\|_2^2, \tag{15}$$

where $\eta > 0$ is the penalty parameter. We group the first two function terms together:

$$\min_{X,Z} \underbrace{\frac{1}{2} \|AX - B\|_2^2 + \lambda \Phi_\gamma(Z)}_{H(X,Z)} + \frac{\eta}{2} \|Z - DX\|_2^2. \tag{16}$$

Simplified iteration to subproblem is given by the following formula:

$$\begin{cases} (X^{k+1}, Z^{k+1}) = \arg\min_{(X,Z)} H(X, Z) + \frac{\eta}{2} \|Z - DX - Y^k\|_2^2 \\ Y^{k+1} = Y^k + (DX^{k+1} - Z^{k+1}) \end{cases}, \tag{17}$$

where k is the number of iterations. Equation (17) can be iteratively solved by splitting it into the minimizations of X and Z, respectively. In this paper, the ABPO-TVSCAD algorithm is divide into three simple alternating Bregman operators steps:

$$\begin{cases} X^{k+1} = \arg\min_{X} \frac{1}{2} \|AX - B\|_2^2 + \frac{\eta}{2} \|Z^k - DX - Y^k\|_2^2 \\ Z^{k+1} = \arg\min_{Z} \lambda \Phi_\gamma(Z) + \frac{\eta}{2} \|Z - DX^{k+1} - Y^k\|_2^2 \\ Y^{k+1} = Y^{k+1} + (DX^{k+1} - Z^{k+1}) \end{cases}. \tag{18}$$

When solving the X-minimization step, we found that it is a quadratic optimization problem, and can be solved via its variational equation:

$$(\eta D^T D + A^T A) X^{k+1} = A^T B + \eta (D^T Z - D^T Y^k). \tag{19}$$

When solving the Z-minimization step, the function Φ_γ is non-differentiable, and we cannot get the optimal solution directly. Therefore, here we consider the corresponding proximity operator of φ_γ as follows:

$$prox_{\varphi_\gamma,\beta}(t) = \arg\min_{x} \varphi_\gamma(x) + \frac{\beta}{2}(x - t)^2 = \begin{cases} sign(t) \max(|t| - \gamma_1, 0), & |t| \leqslant 2\gamma_1 \\ \dfrac{(a-1)t - asign(t)\gamma_1}{a-2}, & 2\gamma_1 < |t| \leqslant \gamma_2, \\ t, & |t| \geqslant \gamma_2 \end{cases} \tag{20}$$

where β is penalty parameter, and $prox_{\varphi_\gamma}(\cdot)$ denotes the Bregman proximity operator. For more details, you can see in Bauschke and Combettes (2011). For the Z-minimization step:

$$\begin{aligned} Z^{k+1} = \arg\min_{Z} \lambda \Phi_\gamma(Z) + \frac{\eta}{2} \|Z - DX^{k+1} - Y^k\|_2^2 = \arg\min_{Z} \Phi_\gamma(Z) \\ + \frac{\eta}{2\lambda} \|Z - (DX^{k+1} + Y^k)\|_2^2. \end{aligned} \tag{21}$$

Through combining equation (20) with equation (21), the following iterative process is generated:

$$\begin{cases} T^k = DX^{k+1} + Y^k \\ Z^{k+1} = prox_{\Phi_\gamma,\rho}(T^k) \end{cases}, \tag{22}$$

where $\rho = \frac{\eta}{\lambda}$.

In our proposed algorithm, we also introduce a strategy of shrinking the PSR to accelerate the convergence of alternating iterations. Details on shrinking the PSR can be seen in Shi *et al* (2014), Guo *et al* (2021). In general, each node of the vector generated by each iteration evaluates their corresponding probability P in the PSR region, and the PSR of the next iteration is divided according to the probability distribution. The calculation method of correlation probability is as follows:

$$\begin{cases} P_{Ed} = \dfrac{1/\|AX - B\|_2^2}{\sum(1/\|AX - B\|_2^2)} \\ P_{Cos} = \dfrac{\sum(AX \cdot B)}{\|AX\|_2 \cdot \|B\|_2} \\ P = \dfrac{P_{Ed} + P_{cos}}{2} \end{cases}, \tag{23}$$

where P_{Ed} is the result of the normalization of the reciprocal of the Euclidean distance, P_{Cos} is the result of the normalization of the reciprocal of the Cosine distance, and P is the result of each reconstruction source distribution corresponding probability weight.

Here, algorithm 1 shows the detailed pseudo code of our proposed ABPO algorithm for solving the TVSCAD model.

Algorithm 1. ABPO-TVSCAD.

Input: system matrix A, measured surface flux photon B.

Initialization: bioluminescent source distribution X^0, the regularization parameter $\lambda = 0.01$, the penalty parameters $\eta = 0.5$, set the parameters $\gamma_1 = 0.03$, $\gamma_2 = a\gamma_1$, $a = 3.7$, and iterator index $k = 0$.

While 1 do

(1): Compute first-order difference matrix.

(2): Alternating Bregman proximity operators.

$$\begin{cases} X^{k+1} = (\eta D^T D + A^T A)^{-1}(A^T B + \eta(D^T Z^k - D^T Y^k)) \\ Z^{k+1} = prox_{\Phi_\gamma,\rho}(DX^{k+1} + Y^k) \\ Y^{k+1} = Y^{k+1} + (DX^{k+1} - Z^{k+1}) \end{cases}$$

(3): Calculate corresponding probability weight according to equation (23).

(4): Judge whether the termination conditions are met.

if $\|AX^k - B\|_2^2 < \|AX^{k+1} - B\|_2^2$ *or* $\sum(AX^k \cdot B) > \sum(AX^{k+1} \cdot B)$ **then**

End while

(5): Dynamically shrink the PSR according to corresponding probability weight.

(6): Increase iteration index.

$k = k + 1$.

Output: $X^* = X^{k-1}$.

3. Experiments and results

In this section, numerical simulations and *in vivo* xenograft mouse experiment were designed to evaluate the performance of ABPO-TVSCAD in BLT reconstruction. The proposed method was compared with the three existing algorithms: conjugated gradient based Tikhonov regularization approach (CG-Tikhonov) (Changqing *et al* 2010), $L1$-based iterative shrinkage (IS- $L1$) (Han *et al* 2010), $L1$-based variable splitting scheme and alternating direction scheme (VSAD- $L1$) (Ye *et al* 2018). The values of the parameters in ABPO-TVSCAD are according to algorithm 1, and the optimal parameter selection details of the other three comparison algorithms are provided in the references (Changqing *et al* 2010, Han *et al* 2010, Ye *et al* 2018). All programs were run on a desktop computer with an Intel(R) Core (TM) i9-12900KF CPU (3.20 GHZ) and 128 GB RAM.

3.1. Experimental process

3.1.1. Numerical simulations

In the numerical simulations, we designed a cylinder model with a radius of 10 mm and height of 30 mm to simulate the body of the organism. Our geometric model was mainly composed of five kinds of organs: heart, bone, liver, lungs, and muscle, as shown in figure 2(a). The optical parameters of each organ at a wavelength of 650 nm were detailed in Cao *et al* (2020). The molecular optical simulations environment (MOSE) (Ren *et al* 2010) based on Monte Carlo method was used to simulate the bioluminescence distribution on tissue surface, and homogeneous density of 1 nw mm^{-3} was used in each source, as shown in figure 2(e). The geometric model was discretized into a uniform tetrahedral mesh by Comsol Multiphysics (Yang *et al* 2015) platform, which included 4626 nodes and 25 840 tetrahedral elements in the reconstruction process, as shown in figure 2(d).

To comprehensively assess the performance of ABPO-SCAD in BLT reconstruction, we designed three groups of numerical simulations. Firstly, a cylindrical source with a radius of 1 mm, a height of 2 mm, and a center coordinate of (6, 3, 24) mm was used to assess the shape recovery ability of ABPO-TVSCAD. The cylindrical source was displayed with red color in 3D view as shown in figure 2(b). Secondly, to evaluate the dual-source reconstruction capability and location accuracy, a dual-source reconstruction simulation was conducted. Two spherical sources with a radius of 1 mm and the central coordinates of the two sources were (0, 0, 19) mm and (0, 0, 25) mm, respectively. Two spherical sources (S1 and S2) were displayed with red color in 3D view as shown in figure 2(c). Thirdly, to evaluate the robustness of our proposed method, we designed an anti-noise simulation. Specifically, 5%, 10%, 15%, 20%, 25% Gaussian noise was added to the surface measurement of a single spherical source with central coordinates (−2, 4, 17) mm. All the source settings in the numerical simulations were listed in table 1.

3.1.2. In vivo *xenograft mouse experiment*

To verify the feasibility of our method *in vivo*, spherical luminescent bead with a radius of 1 mm was implanted into experimental adult nude mouse (about 6–8 weeks old/female). All experimental procedures were approved by the animal ethics committee of the Fourth Military Medical University of China. All animal procedures were performed under isoflurane gas anesthesia (3% isoflurane-air mixture) to minimize suffering to mice. Before *in vivo* BLT reconstruction, the following three steps were implemented.

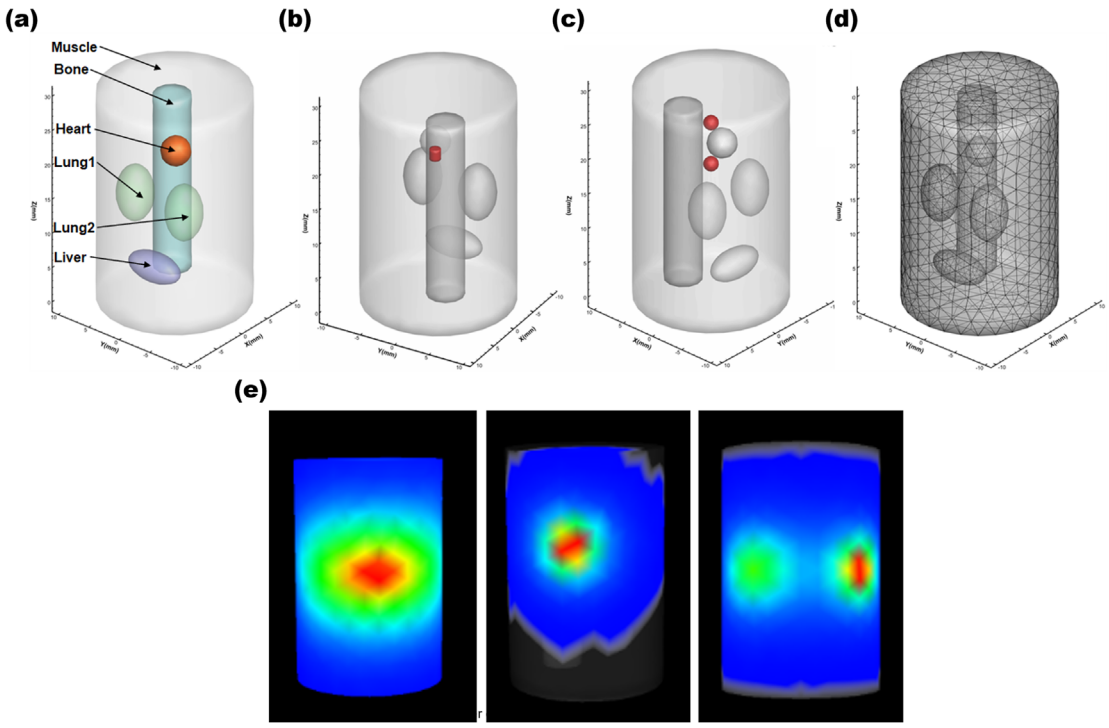

Figure 2. Numerical simulations settings. (a) showed the geometric model for numerical simulations. (b) A cylindrical single source in the geometric model was displayed. (c) Two spherical sources (S1 and S2) in the geometric model were displayed. (d) showed the uniform tetrahedral mesh used in reconstruction. (e) showed the surface bioluminescence distribution (spherical source, cylindrical source, dual-source) with Monte Carlo method.

Table 1. Bioluminescence source setting in numerical simulations.

Simulation	Source shape	Center (mm)	Intensity
Cylindrical	Cylindrical	(6, 3, 24)	1
Anti-noise	Spherical	(−2, 4, 17)	1
Dual-source	Spherical	S1: (0, 0, 19)	1
		S2: (0, 0, 25)	1

Firstly, data collection was carried out. We utilized the dual-mode imaging tomography system to image adult nude mouse, which is composed of luminescence acquisition system (EMCCD camera (iXon Ultra 888), cooled to −80 °C, exposure time of 1 s, no gain value, equipped with Semrock FF01650/10-25 optical filters) and a micro-CT system (tube voltage of 60kvp, x-ray power of 40w). Its schematic illustration was showed in figure 3(a). Consequently, the angle-dependent BLI and micro-CT images of mouse were obtained. Secondly, after the data collection, we proceeded with the data processing. The main organs of the mouse were segmented, including muscle, lung, heart, stomach, liver, and kidney, and then integrated into the mouse trunk model. Thirdly, we matched and registered the bioluminescence image to the surface of the mouse torso model. The structure of *in vivo* experimental data processing was shown in figure 3(b). The coordinate of the implanted real source was (17.5, 21.5, 13.5) mm. The optical parameters of different organs used in the *in vivo* xenograft mouse experiment were from the literature Yi *et al* (2013), as shown in table 2.

3.1.3. Evaluation metrics

To quantitatively analyze the performance of BLT reconstruction, several evaluation metrics were used. The location error (LE) was used to evaluate the localization accuracy. LE is the Euclidean distance between the reconstructed source center and the real source center. The definition is as follows:

$$LE = \|L_{rec} - L_{real}\|_2^2, \tag{24}$$

where L_{rec} denotes the central coordinates of the reconstructed source and L_{real} denotes the central coordinates of the real source. The closer the LE is to 0, the higher the localization accuracy. Dice coefficient was used to assess the similarity between the reconstructed source region and the real source region. The dice is calculated as follows:

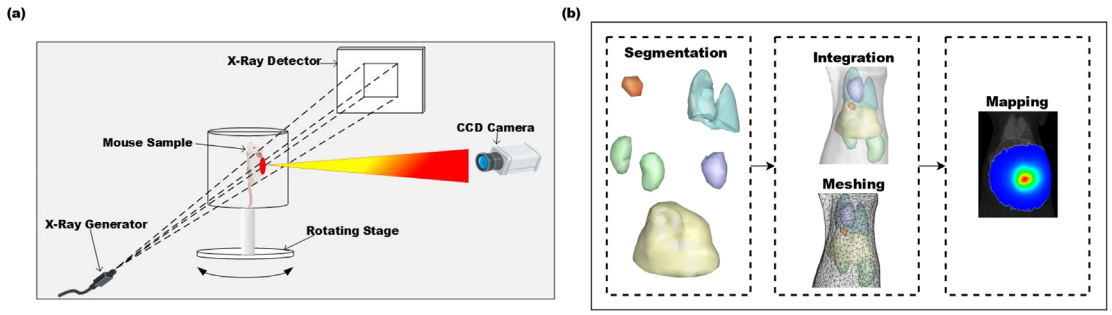

Figure 3. (a) The schematic illustration of the dual-mode imaging tomography system. (b) The structure of *in vivo* xenograft mouse experimental data processing.

Table 2. Optical coefficients used *in vivo* xenograft mouse experiment.

Tissues	$\mu_\alpha(\mathrm{mm}^{-1})$	$\mu_s(\mathrm{mm}^{-1})$	g
Muscle	0.016	0.510	0.90
Heart	0.011	1.053	0.86
Stomach	0.002	1.525	0.90
Liver	0.065	0.723	0.90
Kidney	0.012	2.472	0.90
Lung	0.036	2.246	0.90

$$Dice = \frac{|R_{rec} \cap R_{real}|}{|R_{rec}| + |R_{real}|}, \tag{25}$$

where R_{rec} denotes the reconstructed source region and R_{real} denotes the real source region. The closer the dice is to 1, the higher the similarity between the reconstructed source region and the real source region. The relative intensity error (RIE) is used to evaluate the relative intensity deviation between the reconstruction source intensity and the real source intensity. The RIE is calculated as follows:

$$RIE = \frac{|I_{real} - I_{rec}|}{I_{rec}}, \tag{26}$$

where I_{rec} denotes the mean intensity of the reconstruction source and I_{real} denotes the mean intensity of the real source. If the RIE is closer to 0, the intensity recovery of the reconstructed source is better.

3.2. Results

3.2.1. Cylindrical single-source simulation reconstruction

To measure the shape recovery ability of our proposed method, we compared the reconstruction performance of ABPO-TVSCAD with other methods using cylindrical single source. The 3D mesh of the reconstructed source obtained by these methods was shown in figure 4(a). The results showed that the source shape reconstructed by ABPO-TVSCAD is more accurate than other methods and more similar to the shape of the real source. CG-Tikhonov produces over-smooth source boundaries, while IS-$L1$ generates over-convergent source boundaries. Although the results obtained by VASAD-$L1$ are satisfactory, our method produced fewer artifacts and exhibited a superior overlap with the real source mesh, with dice of 0.894. In addition, the LE and RIE obtained by our method were smallest (figure 4(b)), which demonstrated that our method showed best location accuracy and source intensity recovery. The quantitative analysis of the cylindrical single-source simulation reconstruction was shown in table 3.

3.2.2. Spherical dual-source simulation reconstruction

To assess the localization accuracy and dual-source reconstruction ability of ABPO-TVSCAD, we compared the reconstruction performance of ABPO-TVSCAD with other methods mentioned above. The reconstruction results obtained by dual-source simulation using different methods were shown in figure 5. The representation of real and reconstructed sources in 3D views and in the slice views were similar to that of cylindrical source simulation. By observing the shapes of 3D view, axial view, coronal view, and sagittal view, it was obvious that our method was effective and accurate. Compared with other methods, the position of the reconstructed sources by ABPO-TVSCAD approach were closer to the real sources center. The performance of the reconstructed

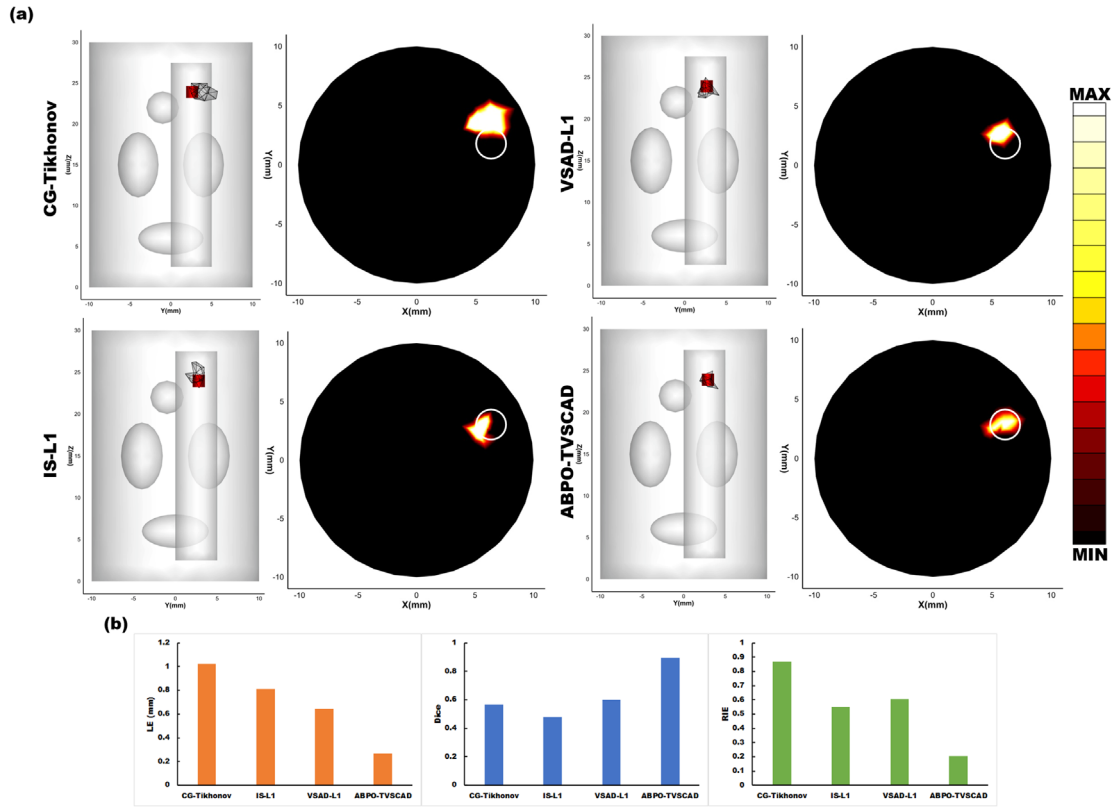

Figure 4. Results of cylindrical single-source simulation reconstruction. (a) The 3D view and axial view of bioluminescent source were reconstructed by four different methods. The real source was depicted with a red cylinder and the reconstructed region was shown with the black meshes under 3D view. The white circles on the plane view indicate the real source under the axial view. (b) The results of the evaluation indicators of the four methods.

Table 3. Quantitative comparison in cylindrical source reconstruction.

Method	Real central position (mm)	Reconstructed central position (mm)	LE (mm)	Dice	RIE
CG-Tikhonov	(6, 3, 24)	(5.21, 3.64, 23.90)	1.02	0.56	0.67
IS-*L*1	(6, 3, 24)	(5.33, 2.60, 24.23)	0.81	0.48	0.55
VASAD-*L*1	(6, 3, 24)	(5.60, 2.65, 23.64)	0.64	0.60	0.60
ABPO-TVSCAD	(6, 3, 24)	(6.18, 2.90, 23.83)	0.27	0.89	0.20

localization of CG-Tikhonov and IS-*L*1 was unsatisfactory. The reconstruction results of VSAD-*L*1 were better than those of the two methods. In addition, the quantitative analysis results shown in table 4 showed that ABPO-TVSCAD performed best. The results showed that compared with the other three methods, the ABPO-TVSCAD method successfully improved the dual-source reconstruction capability and location accuracy.

3.2.3. Anti-noise ability test

To test the robustness of the ABPO-TVSCAD method, we added 5%, 10%, 15%, 20%, 25% Gaussian noise to the measured surface luminous flux of the spherical single-source with a radius of 1 mm. The evaluation metrics results of ABPO-TVSCAD for the reconstruction of sources with different ratio of Gaussian noise was shown in figure 6. It was observed that when the ratio of Gaussian noise changed, the variation range of the evaluation metrics were relatively stable. The results showed that the robustness of APBO-TVSCAD method was superb.

3.2.4. Reconstruction of the in vivo *xenograft mouse*

To evaluate the practicability of our method *in vivo* imaging, we performed *in vivo* xenograft mouse experiment. It should be noted here that the evaluation index RIE cannot be obtained because the grayscale image and internal source of the surface detection are not calibrated with the actual number of photons. The 3D view and axial slice view of reconstruction results verified the effectiveness of different methods, as shown in figure 7(c). The white circles in the slice view represent the location and shape of the implanted bioluminescent bead. The performance of the four BLT reconstruction approaches was relatively consistent with those obtained by

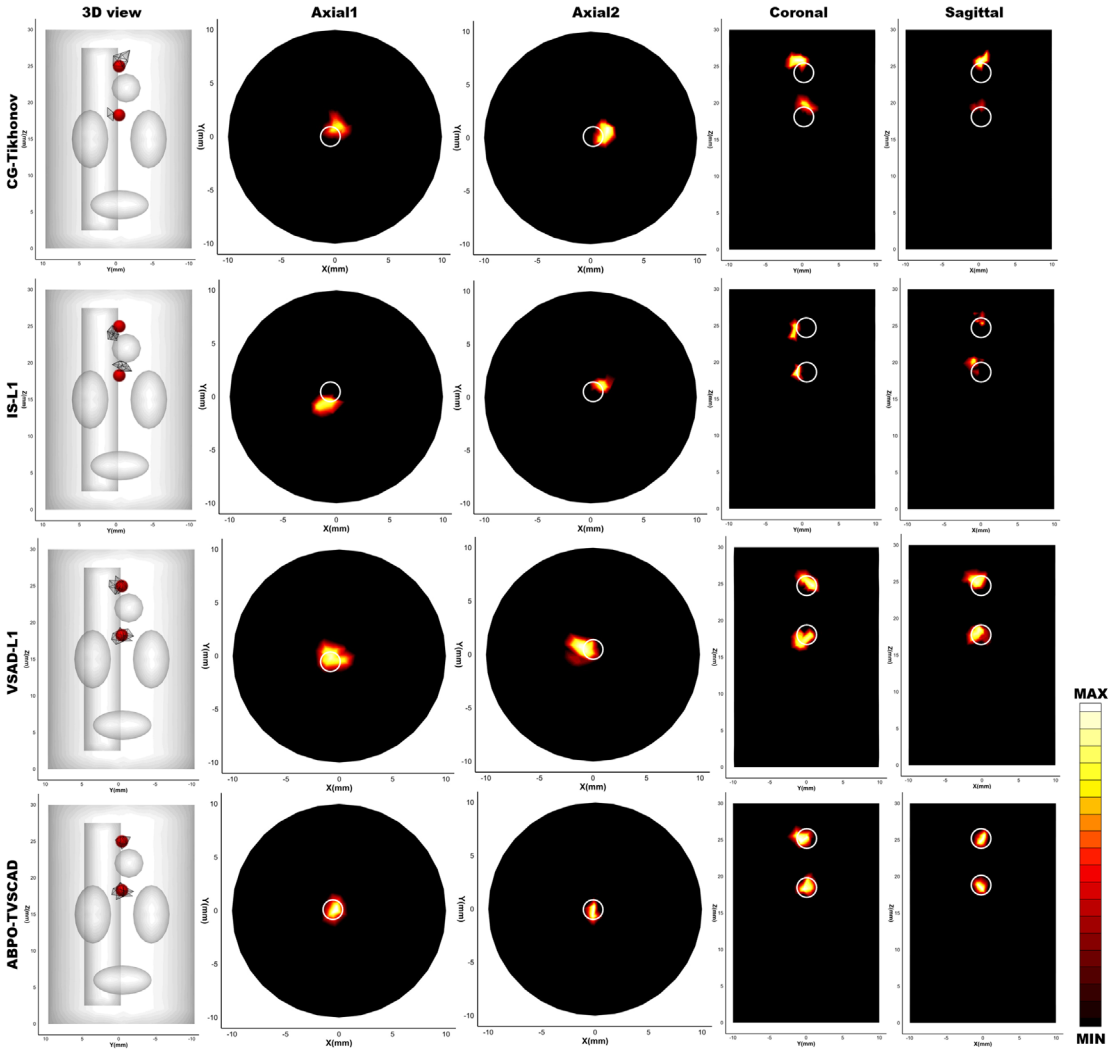

Figure 5. Reconstruction results of different methods for dual-source. The real sources were depicted with red spheres under 3D view and the white circles on the plane view indicate the real source location and shape.

Table 4. Quantitative comparison in cylindrical source reconstruction.

Method	Real central position (mm)	Reconstructed central position (mm)	LE (mm)	Total LE (mm)	Dice	RIE
CG-Tikhonov	(0, 0, 19)	(0.25, 0.96, 18.43)	1.14	2.12	0.41	0.58
	(0, 0, 25)	(0.39, −0.64, 25.81)	0.98		0.43	0.53
IS-*L*1	(0, 0, 19)	(−0.96, −0.56, 19.38)	1.18	2.35	0.44	0.49
	(0, 0, 25)	(0.44, 0.71, 24.18)	1.17		0.37	0.42
VASAD-*L*1	(0, 0, 19)	(−0.49, −0.04, 18.28)	0.87	1.86	0.51	0.42
	(0, 0, 25)	(−0.85, 0.50, 25.04)	0.99		0.62	0.58
ABPO-TVSCAD	(0, 0, 19)	(−0.28, −0.05,18.74)	0.39	0.81	0.84	0.20
	(0, 0, 25)	(−0.06, −0.38, 25.17)	0.42		0.74	0.13

numerical simulations. As shown in table 5, compared with the other three methods, ABPO-TVSCAD method showed the minimum LE value and the maximum dice value. These results indicated that ABPO-TVSCAD method possessed the most superior practicality *in vivo* xenograft mouse experiment.

4. Discussion and conclusion

BLT is a promising three-dimensional imaging method, which can solve the problem of insufficient depth resolution of BLI by reconstructing three-dimensional bioluminescence distribution. However, the severe ill-conditioned inverse problem restricts the performance of reconstruction. In this study, ABPO-TVSCAD

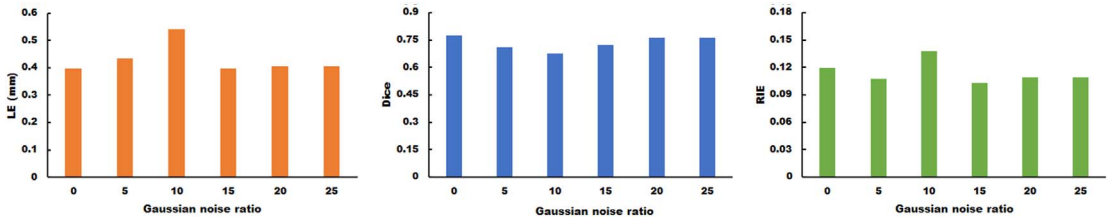

Figure 6. The evaluation metrics results of ABPO-TVSCAD for anti-noise ability test.

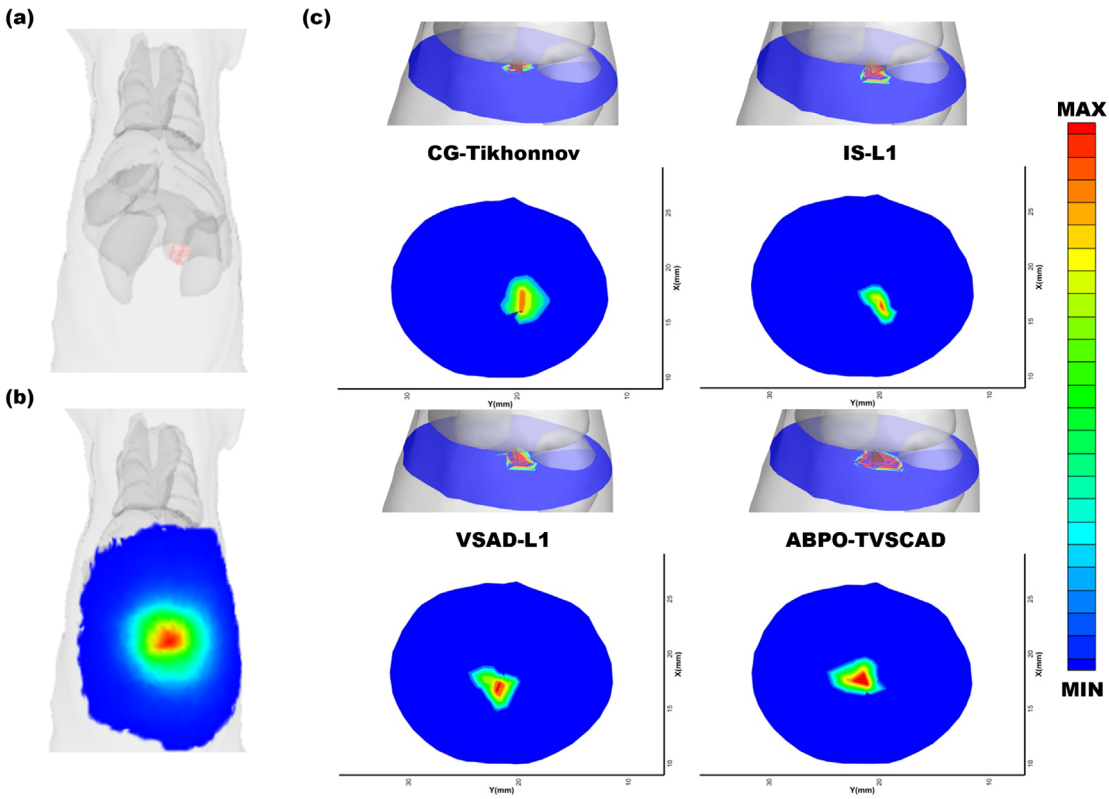

Figure 7. *In vivo* xenograft mouse experiment of single light source. (a) The 3D view of real source in the mouse. Real light sources were represented by red spheres. (b) The surface photon distribution. (c) The reconstructions by different methods under the 3D view (a partial body in (b)) and the axial view results. The white outline denoted the location and shape of the real source.

Table 5. Quantitative comparison for reconstruction of the *in vivo* xenograft mouse.

Method	Real central position (mm)	Reconstructed central position (mm)	LE (mm)	Dice
CG-Tikhonov	(17.5, 21.5, 13.5)	(16.63, 21.21, 13.76)	0.95	0.45
IS-*L*1	(17.5, 21.5, 13.5)	(17.89, 21.74, 14.29)	0.92	0.57
VASAD-*L*1	(17.5, 21.5, 13.5)	(17.00, 21.44, 13.88)	0.67	0.72
ABPO-TVSCAD	(17.5, 21.5, 13.5)	(17.61, 21.52, 13.70)	0.23	0.91

reconstructed method was proposed to alleviate the ill-posedness and improve the performance of BLT reconstruction. Firstly, TVSCAD regularization is proposed to balance the sparsity and edge preservation of the source, and the objective optimization function is constructed based on TVSCAD regularization. Secondly, since our objective function is non-differentiable, inspired by split Bregman algorithm, the objective function is decomposed into a differentiable operator and a Bregman proximal operator for alternate solution. Then, we add non-negative constraints to the alternate solution process to reduce the error. Finally, in order to accelerate the convergence of the solution, we utilize the strategy of shrinking PSR.

Three groups of numerical simulations and one group of *in vivo* xenograft mouse experiment were performed to verify the performance of ABPO-TVSCAD, and quantitative comparisons were made with CG-Tikhonov, IS-$L1$, and VSAD-$L1$. The results of experiments were shown as follows. Firstly, the cylindrical single source simulation revealed that ABPO-TVSCAD possessed superior source recovery capability compared with other methods mentioned above. Secondly, dual-source simulation indicated that ABPO-TVSCAD had excellent dual-source reconstruction capability and high spatial positioning accuracy. Thirdly, the anti-noise test proved the robustness of our proposed method. Finally, *in vivo* xenograft mouse experiment demonstrated the practicability of ABPO-TVSCAD for luminescence detection in living animals and its potential for BLT reconstruction in preclinical studies.

Regardless of ABPO-TVSCAD strategy has superior performance in BLT reconstruction, the method still has some drawbacks. Firstly, when determining the objective function, the regularization parameters used are selected according to experience, and the optimal parameters cannot be determined automatically. The further study is needed on how to determine parameters automatically. Furthermore, as with most of BLT reconstruction of traditional numerical methods, our system matrix A still has some bias. An adaptive method to determine the system matrix need to be developed in the future. In addition, the performance of ABPO-TVSCAD requires further validation in preclinical application for other optical tomography techniques.

In conclusion, we propose an ABPO-TVSCAD method to improve the performance of BLT. The algorithm combines the advantages of TV regularization and SCAD regularization, and balances the sparsity and morphological reservation of reconstructed BLT reconstruction. The algorithm was verified by a series of numerical simulations and *in vivo* xenograft mouse experiment. Compared with several conventional numerical methods, ABPO-TVSCAD method performed superior in spatial localization accuracy, shape recovery capability, dual-source reconstructed capability. We believe that this approach can contribute to the study of various preclinical applications of BLT and promote theoretical research in optical molecular imaging.

Acknowledgments

This work was supported in part by the National Key Research and Development Program of China (2019YFC1521102); National Natural Science Foundation of China (61701403, 61806164, 62101439, 61906154); China Postdoctoral Science Foundation (2018M643719); Natural Science Foundation of Shaanxi Province (2020JQ-601); Young Talent Support Program of the Shaanxi Association for Science and Technology (20190107); Key Research and Development Program of Shaanxi Province (2019GY-215, 2021ZDLSF06-04); Major research and development project of Qinghai (2020-SF-143).

ORCID iDs

Xin Cao https://orcid.org/0000-0003-3560-6523

References

Baraniuk R G, Cevher V, Duarte M F and Hegde C 2010 Model-based compressive sensing *IEEE Trans. Inf. Theory* **56** 1982–2001

Bauschke H H and Combettes P L 2011 *Convex Analysis and Monotone Operator Theory in Hilbert Spaces* vol 408 (Berlin: Springer)

Cao X, Wei X, Yan F, Wang L, Su L, Hou Y, Geng G and He X 2019 A novel stacked denoising autoencoder-based reconstruction framework for cerenkov luminescence tomography *IEEE Access* **7** 85178–89

Cao X, Zhang J, Yang J, Fan C, Zhao F, Zhou W, Wang L, Geng G, Zhou M and Chen X 2020 A deep unsupervised clustering-based post-processing framework for high-fidelity Cerenkov luminescence tomography *J. Appl. Phys.* **128** 193104

Changqing L *, Mitchell G S and Cherry S R 2010 Cerenkov luminescence tomography for small-animal imaging *Opt. Lett.* **35** 1109–11

Cong W and Wang G 2006 Boundary integral method for bioluminescence tomography *J. Biomed. Opt.* **11** 020503

Darne C, Lu Y and Sevick-Muraca E M 2013 Small animal fluorescence and bioluminescence tomography: a review of approaches, algorithms and technology update *Phys. Med. Biol.* **59** R1

Dehghani H, Guggenheim J A, Taylor S L, Xu X and Wang K K-H 2018 Quantitative bioluminescence tomography using spectral derivative data *Biomed. Opt. Express* **9** 4163–74

Fan J and Li R 2001 Variable selection via nonconcave penalized likelihood and its oracle properties *J. Am. Stat. Assoc.* **96** 1348–60

Feng J, Jia K, Li Z, Pogue B W, Yang M and Wang Y 2018 Bayesian sparse-based reconstruction in bioluminescence tomography improves localization accuracy and reduces computational time *J. Biophoton.* **11** e201700214

Feng J, Qin C, Jia K, Zhu S, Yang X and Tian J 2011 Bioluminescence tomography imaging *in vivo*: recent advances *IEEE J. Sel. Top. Quantum Electron.* **18** 1394–402

Gao Y, Wang K, An Y, Jiang S, Meng H and Tian J 2018 Nonmodel-based bioluminescence tomography using a machine-learning reconstruction strategy *Optica* **5** 1451–4

Gong R, Cheng X and Han W 2018 A homotopy method for bioluminescence tomography *Inverse Prob. Sci. Eng.* **26** 398–421

Gu G, Jiang S and Yang J 2017 A TVSCAD approach for image deblurring with impulsive noise *Inverse Prob.* **33** 125008

Guo H, Gao L, Yu J, He X, Wang H, Zheng J and Yang X 2020 Sparse-graph manifold learning method for bioluminescence tomography *J. Biophoton.* **13** e201960218

Guo H, Yu J, He X, Yi H, Hou Y and He X 2022 Total variation constrained graph manifold learning strategy for cerenkov luminescence tomography *Opt. Express* **30** 1422–41
Guo H, Yu J, Hu Z, Yi H, Hou Y and He X 2018 A hybrid clustering algorithm for multiple-source resolving in bioluminescence tomography *J. Biophoton.* **11** e201700056
Guo H, Zhao H, Yu J, He X, He X and Song X 2021 X-ray luminescence computed tomography using a hybrid proton propagation model and Lasso-LSQR algorithm *J. Biophoton.* **14** e202100089
Guo L, Liu F, Cai C, Liu J and Zhang G 2019 3D deep encoder–decoder network for fluorescence molecular tomography *Opt. Lett.* **44** 1892–5
Han D, Tian J, Zhu S, Feng J, Qin C, Zhang B and Yang X 2010 A fast reconstruction algorithm for fluorescence molecular tomography with sparsity regularization *Opt. Express* **18** 8630–46
Han W, Cong W and Wang G 2006 Mathematical theory and numerical analysis of bioluminescence tomography *Inverse Prob.* **22** 1659
He X, Liang J, Wang X, Yu J, Qu X, Wang X, Hou Y, Chen D, Liu F and Tian J 2010 Sparse reconstruction for quantitative bioluminescence tomography based on the incomplete variables truncated conjugate gradient method *Opt. Express* **18** 24825–41
Herman G T and Davidi R 2008 Image reconstruction from a small number of projections *Inverse Prob.* **24** 045011
Hintermüller M, Holler M and Papafitsoros K 2018 A function space framework for structural total variation regularization with applications in inverse problems *Inverse Prob.* **34** 064002
Huang C, Meng H, Gao Y, Jiang S X and Tian J 2019 *Imaging, Manipulation, and Analysis of Biomolecules, Cells, and Tissues XVII)*, vol. Series)
Jianghong Z, Jie T, Xin, Yang C and Qin 2011 Whole-body cerenkov luminescence tomography with the finite element SP3 method *Ann. Biomed. Eng.* **39** 1728–35
Klose A D, Beattie B J, Dehghani H, Vider L, Le C, Ponomarev V and Blasberg R 2010 *In vivo* bioluminescence tomography with a blocking-off finite-difference SP3 method and MRI／CT coregistration *Med. Phys.* **37** 329–38
Klose A D and Larsen E W 2006 Light transport in biological tissue based on the simplified spherical harmonics equations *J. Comput. Phys.* **220** 441–70
Leng C and Tian J 2015 Mathematical method in optical molecular imaging *Sci. China Inf. Sci.* **58** 1–13
Li D, Chen C, Li J and Yan Q 2020 Reconstruction of fluorescence molecular tomography based on graph convolution networks *J. Opt.* **22** 045602
Li S, He X, Zhang H, Guo H and He X 2021 *43rd Annual Int. Conf. of the IEEE Engineering in Medicine & Biology Society (EMBC),2021)* (IEEE) vol. Series pp 3634–9
Ma X, Tian J, Qin C, Yang X, Zhang B, Xue Z, Zhang X, Han D, Dong D and Liu X 2011 Early detection of liver cancer based on bioluminescence tomography *Appl. Opt.* **50** 1389–95
Massoud T F and Gambhir S S 2003 Molecular imaging in living subjects: seeing fundamental biological processes in a new light *Genes Dev.* **17** 545–80
Naser M A and Patterson M S 2010 Algorithms for bioluminescence tomography incorporating anatomical information and reconstruction of tissue optical properties *Biomed. Opt. Express* **1** 512–26
Ntziachristos V 2010 Going deeper than microscopy: the optical imaging frontier in biology *Nat. Methods* **7** 603–14
Qin C, Feng J, Zhu S, Ma X, Zhong J, Wu P, Jin Z and Tian J 2014 Recent advances in bioluminescence tomography: methodology and system as well as application *Laser Photon. Rev.* **8** 94–114
Qin C, Zhu S, Feng J, Zhong J, Ma X, Wu P and Tian J 2011 Comparison of permissible source region and multispectral data using efficient bioluminescence tomography method *J. Biophoton.* **4** 824–39
Ren N, Liang J, Qu X, Li J, Lu B and Tian J 2010 GPU-based Monte Carlo simulation for light propagation in complex heterogeneous tissues *Opt. Express* **18** 6811–23
Ring W 2000 Structural properties of solutions to total variation regularization problems *ESAIM: Math. Modelling Numer. Anal.* **34** 799–810
Shi J, Liu F, Zhang G, Luo J and Bai J 2014 Enhanced spatial resolution in fluorescence molecular tomography using restarted L1-regularized nonlinear conjugate gradient algorithm *J. Biomed. Opt.* **19** 046018
Wang G, Li Y and Jiang M 2004 Uniqueness theorems in bioluminescence tomography *Med. Phys.* **31** 2289–99
Wang J, Ma J, Han B and Li Q 2012 Split Bregman iterative algorithm for sparse reconstruction of electrical impedance tomography *Signal Process.* **92** 2952–61
Wang M, Song L and Tian G-L 2015 SCAD-penalized least absolute deviation regression in high-dimensional models *Commun. Stat.-Theory Methods* **44** 2452–72
Wang T, Nakamoto K, Zhang H and Liu H 2017 Reweighted anisotropic total variation minimization for limited-angle CT reconstruction *IEEE Trans. Nucl. Sci.* **64** 2742–60
Wenxiang C, Wang D, Kumar L, Ming J, Lihong and Eric 2005 Practical reconstruction method for bioluminescence tomography *Opt. Express* **13** 6756–71
Wu P, Hu Y, Wang K and Tian J 2013 Bioluminescence tomography by an iterative reweighted (l) 2 norm optimization *IEEE Trans. Biomed. Eng.* **61** 189–96
Wu P, Liu K, Zhang Q, Xue Z, Li Y, Ning N, Yang X, Li X and Tian J 2012 Detection of mouse liver cancer via a parallel iterative shrinkage method in hybrid optical/microcomputed tomography imaging *J. Biomed. Opt.* **17** 126012
Xu X, Deng Z, Dehghani H, Iordachita I, Lim M, Wong J W and Wang K K-H 2021 Quantitative bioluminescence tomography-guided conformal irradiation for preclinical radiation research *Int. J. Radiat. Oncol.* Biol.* Phys.* **111** 1310–21
Yang D, Yan C, Yang L, Peng D and Chen X 2018 An alternative reconstruction framework with optimal permission source region for bioluminescence tomography *Opt. Commun.* **427** 112–22
Yang Y, Wang K K H, Eslami S, Iordachita I I, Patterson M S and Wong J W 2015 Systematic calibration of an integrated x-ray and optical tomography system for preclinical radiation research *Med. Phys.* **42** 1710–20
Ye J, Du Y, An Y, Mao Y, Jiang S, Shang W, He K, Yang X, Wang K and Chi C 2018 Sparse reconstruction of fluorescence molecular tomography using variable splitting and alternating direction scheme *Mol. Imaging Biol.* **20** 37–46
Yi H, Chen D, Li W, Zhu S, Wang X, Liang J and Tian J 2013 Reconstruction algorithms based on l1-norm and l2-norm for two imaging models of fluorescence molecular tomography: a comparative study *J. Biomed. Opt.* **18** 056013
Yin L, Wang K, Tong T, An Y, Meng H, Yang X and Tian J 2019 Improved block sparse bayesian learning method using k-nearest neighbor strategy for accurate tumor morphology reconstruction in bioluminescence tomography *IEEE Trans. Biomed. Eng.* **67** 2023–32
Yin L, Wang K, Tong T, Wang Q, An Y, Yang X and Tian J 2021 Adaptive grouping block sparse bayesian learning method for accurate and robust reconstruction in bioluminescence tomography *IEEE Trans. Biomed. Eng.* **68** 3388–98
Yu J, Liu F, Wu J, Jiao L and He X 2010 Fast source reconstruction for bioluminescence tomography based on sparse regularization *IEEE Trans. Biomed. Eng.* **57** 2583–6